

## *Herschel* SPIRE discovery of far-infrared excess synchrotron emission from the west hot spot of the radio galaxy Pictor A.

NAOKI ISOBE,<sup>1</sup> YUJI SUNADA,<sup>2</sup> MOTOKI KINO,<sup>3,4</sup> SHOKO KOYAMA,<sup>5</sup> MAKOTO TASHIRO,<sup>1,2</sup> HIROSHI NAGAI,<sup>4,6</sup> AND CHRIS PEARSON<sup>7,8,9</sup>

<sup>1</sup> *Institute of Space and Astronautical Science (ISAS), Japan Aerospace Exploration Agency (JAXA), 3-1-1 Yoshinodai, Chuo-ku, Sagami-hara, Kanagawa, 252-5210, Japan*

<sup>2</sup> *Department of Physics, Saitama University, 255 Shimo-Okubo, Sakura-ku, Saitama, 338-8570, Japan*

<sup>3</sup> *Kogakuin University of Technology & Engineering, Academic Support Center, 2665-1 Nakano, Hachioji, Tokyo, 192-0015, Japan*

<sup>4</sup> *National Astronomical Observatory of Japan, 2-21-1 Osawa, Mitaka, Tokyo, 181-8588, Japan*

<sup>5</sup> *Academia Sinica Institute of Astronomy and Astrophysics, PO Box 23-141, Taipei 10617, Taiwan*

<sup>6</sup> *The Graduate University for Advanced Studies (SOKENDAI), Osawa 2-21-1, Mitaka, Tokyo, 181-8588, Japan*

<sup>7</sup> *RAL Space, STFC Rutherford Appleton Laboratory, Didcot, Oxfordshire, OX11 0QX, UK*

<sup>8</sup> *Oxford Astrophysics, University of Oxford, Keble Rd, Oxford OX1 3RH, UK*

<sup>9</sup> *Department of Physical Sciences, The Open University, Milton Keynes, MK7 6AA, UK*

(Received —; Revised —; Accepted —)

### ABSTRACT

A far-infrared counterpart to the west hot spot of the radio galaxy Pictor A is discovered with the Spectral and Photometric Imaging REceiver (SPIRE) onboard *Herschel*. The color-corrected flux density of the source is measured as  $70.0 \pm 9.9$  mJy at the wavelength of  $350 \mu\text{m}$ . A close investigation into its radio-to-optical spectrum indicates that the mid-infrared excess over the radio synchrotron component, detected with *WISE* and *Spitzer*, significantly contributes to the far-infrared band. Thanks to the SPIRE data, it is revealed that the spectrum of the excess is described by a broken power-law model subjected to a high-energy cutoff. By applying the radiative cooling break under continuous energy injection ( $\Delta\alpha = 0.5$ ), the broken power-law model supports an idea that the excess originates in 10-pc scale substructures within the hot spot. From the break frequency,  $\nu_b = 1.6_{-1.0}^{+3.0} \times 10^{12}$  Hz, the magnetic field was estimated as  $B \simeq 1\text{--}4$  mG. This is higher than the minimum-energy magnetic field of the substructures by a factor of 3–10. Even if the origin of the excess is larger than  $\sim 100$  pc, the magnetic field stronger than the minimum-energy field is confirmed. It is proposed that regions with a magnetic field locally boosted via plasma turbulence are observed as the substructures. The derived energy index below the break,  $\alpha \sim 0.22$  (conservatively  $< 0.42$ ), is difficult to be attributed to the strong-shock acceleration ( $\alpha = 0.5$ ). Stochastic acceleration and magnetic reconnection are considered as a plausible alternative mechanism.

*Keywords:* galaxies: jets — galaxies: individual (Pictor A) — infrared: galaxies — radiation mechanisms: non-thermal — acceleration of particles

### 1. INTRODUCTION

Compact radio hot spots hosted by Fanaroff-Riley type-II (FR-II; Fanaroff & Riley 1974) radio galaxies are widely associated with a strong shock at the terminal of their nuclear jets (e.g., Begelman et al. 1984). The existence of high-energy electrons in the hot spots, ac-

celerated by the shock via the first-order Fermi process, is observationally evidenced by their bright synchrotron radio emission and inverse-Compton X-ray one (e.g., Hardcastle et al. 2004). These make the hot spots one of the possible generators of high-energy cosmic rays (e.g., Meisenheimer et al. 1989, 1997). For detailed investigation of the acceleration phenomena in the hot spots, it is necessary to put observational constraints on the physical parameters, such as the magnetic field strength, by making use of the multi-frequency spectrum.

The radio and X-ray spectral energy distributions of the hot spots are typically described by a simple one-zone synchrotron-self-Compton (SSC) model. The magnetic field in the hot spots estimated by the SSC model is usually consistent to the minimum-energy and/or equipartition value (e.g., [Hardcastle et al. 2004](#); [Kataoka & Stawartz 2005](#)). However, the spectrum of low-luminosity objects tends to deviate from the one-zone SSC model. By pioneering mid-infrared (MIR) studies with *Spitzer*, a hint of a multi-synchrotron scenario was given to several low-luminosity hot spots (e.g., [Kraft et al. 2007](#); [Werner et al. 2012](#)), and also to some jet knots (e.g., [Uchiyama et al. 2006](#)). Thus, the acceleration phenomena in the hot spots are suggested to be more complicated and inhomogeneous in comparison to the standard picture of the strong shock acceleration.

The prototypical FR II radio galaxy Pictor A ([Perley et al. 1997](#)), located at the redshift of  $z = 0.035$  ([Eracleous & Halpern 2004](#)), provides an ideal laboratory for an observational study of the particle acceleration in the hot spots. The west hot spot of this radio galaxy is one of the brightest and most extensively studied low-luminosity hot spots in a variety of frequency ranges from the radio to X-ray bands (e.g., [Thomson et al. 1995](#); [Meisenheimer et al. 1997](#); [Tingay et al. 2008](#); [Wilson et al. 2001](#); [Werner et al. 2012](#)). Because the X-ray spectrum of the object is reported to be unaccountable by the one-zone SSC model, a number of the multi-synchrotron ideas were invoked (e.g., [Wilson et al. 2001](#); [Tingay et al. 2008](#)).

In addition, a new spectral component was identified from the west hot spot of Pictor A in the MIR band ([Isobe et al. 2017](#)). From a careful analysis of the MIR data obtained with the Wide-field Infrared Survey Explorer (*WISE*), a significant MIR excess was unveiled over the power-law (PL) like extrapolation of the synchrotron radio spectrum smoothly connecting to the optical one. By adopting a naive cutoff-PL model to the excess, a number of important implications are derived by [Isobe et al. \(2017\)](#). Firstly, they proposed that the MIR excess originates in the 10-pc scale substructures within the hot spot resolved by the Very Long Baseline Array (VLBA, [Tingay et al. 2008](#)). Secondly, the magnetic field in the substructures are possible to be amplified via some plasma effects in comparison to the minimum-energy field. Thirdly, they hinted that the spectrum of the excess (the energy index of  $\alpha \sim 0.4$ ) is harder than the prediction of the strong shock acceleration ( $\alpha = 0.5$ ). However, the detailed investigation into the spectrum of the excess has remained yet unexplored, due to the wavelength gap between the radio and MIR bands.

In order to precisely specify the physical condition for the electron acceleration of the excess, it is indispensable to determine precisely its spectral shape. The *Herschel* space observatory ([Pilbratt et al. 2010](#)) has a potential to tackle this issue, since it is able to widely cover the far-infrared (FIR) range with a wavelength of  $\lambda = 60\text{--}670 \mu\text{m}$ , corresponding to the frequency of  $\nu = (0.45\text{--}5) \times 10^{12}$  Hz. It is found that the west hot spot of Pictor A was serendipitously mapped with the Spectral and Photometric Imaging REceiver (SPIRE; [Griffin et al. 2010](#)) onboard *Herschel* at its three photometric bands with an effective wavelength of  $\lambda = 250, 350$  and  $500 \mu\text{m}$ . On these SPIRE maps, an FIR source is discovered at the position of the hot spot. The SPIRE data, in combination with the previous multi-wavelength ones, make possible a detailed re-examination on the spectrum of the excess and on its physical interpretation.

In the following, the cosmological constants same as those in [Tingay et al. \(2008\)](#) and [Isobe et al. \(2017\)](#) are employed for mutual consistency;  $H_0 = 71 \text{ km s}^{-1} \text{ Mpc}^{-1}$ ,  $\Omega_m = 0.27$ , and  $\Omega_\Lambda = 0.73$  ([Spergel et al. 2003](#)). Under this cosmology, an angular size of  $1''$  corresponds to a physical size of 688 pc at the rest frame of Pictor A ( $z = 0.035$ ).

## 2. FIR DATA WITH THE *Herschel* SPIRE

### 2.1. Observation and Analysis

The nucleus of the FR-II radio galaxy Pictor A was previously targeted by the *Herschel* space observatory on three occasions. In one observation conducted with the SPIRE photometer in the small-map mode on 2011 September 22 (Obs. ID = 1342229235), the west hot spot of Pictor A was serendipitously mapped. In the remaining two observations, in which the Photodetector Array Camera and Spectrometer (PACS; [Poglitsch et al. 2010](#)) was operated in the photometer scan-map mode, the object was unfortunately located outside the PACS field of view.

The present study focuses on the SPIRE observation of Pictor A. The final version of the SPIRE science data were obtained from the *Herschel* Science Archive. The Levels 1 and 2 products of the SPIRE data were analyzed with the version 15.0.1 of the *Herschel* Interactive Processing Environment (HIPE) by referring to the latest version of the calibration tree (`spire_cal_14_3`).

In order to carry out detection and position determination of FIR point sources on the SPIRE map, the HIPE tool SUSSExtractor (`sourceExtractorSussextractor`) was adopted. Photometry of the detected sources was performed with the SPIRE Timeline Fitter (`sourceExtractorTimeline`) in

the standard manner. This method is reported to be most reliable among the four major photometric procedures implemented by the HIPE for a point source brighter than  $\sim 30$  mJy (Pearson et al. 2014). The source coordinates determined with the SUSSEXtractor were employed as a reference position for the SPIRE Timeline Fitter. It was confirmed that the photometric results with the SPIRE Timeline Fitter and SUSSEXtractor become consistent to each other within a difference of  $\lesssim 10\%$ , which is smaller than the photometric error at all the three SPIRE bands.

## 2.2. Result

The SPIRE Level-2 point-source maps (`psrcPMW`) around the nucleus and west hot spot of Pictor A are compared in the left and right panels of Figure 1, respectively, with the radio image obtained with the Australia Telescope Compact Array (ATCA) at the 4.8 GHz band (Isobe et al. 2017, the original data were kindly provided by Dr. E. Lenc, private communication). Although the spatial resolution is highest at  $250 \mu\text{m}$  among the three SPIRE photometric bands, the significance of the FIR source corresponding to the west hot spot is relatively low at this band (see below). Thus, the SPIRE images at the wavelength of  $350 \mu\text{m}$  are utilized here.

The left panel of Figure 1 clearly displays that FIR emission is detected from the nucleus with a  $350 \mu\text{m}$  color-uncorrected flux density of  $618 \pm 7$  mJy. The SPIRE position of the nucleus at  $350 \mu\text{m}$ , indicated with the cross in the left panel of Figure 1, coincides well with its 4.8 GHz ATCA peak within the SPIRE astrometric uncertainty ( $\sim 2''$ ; Swinyard et al. 2010).

An FIR source spatially associated with the west hot spot of Pictor A is clearly found on the  $350 \mu\text{m}$  SPIRE image shown in the right panel of Figure 1. This FIR source is significantly detected at all the three SPIRE photometric bands with a signal-to-noise ratio of 4.6, 7.1 and 10.7 at 250, 350 and  $500 \mu\text{m}$ , respectively. The sky position of the SPIRE source, indicated by the cross in the right panel of Figure 1, is found to show a reasonable coincidence to the ATCA position of the west hot spot, within the SPIRE astrometric accuracy. Thus, in the following, the SPIRE source is regarded as the real FIR counterpart of the west hot spot.

Table 1 summarizes the SPIRE photometry of the west hot spot performed with the Timeline Fitter. The color-corrected FIR flux density of the object was derived as  $F_\nu = 70.0 \pm 9.9$  mJy at  $350 \mu\text{m}$ . The color-correction factor  $f_{\text{col}}$  was taken from the SPIRE calibration tree by assuming the energy index of  $\alpha = 1.1$  ( $F_\nu \propto \nu^{-\alpha}$ ). The adopted index was found to be self-consistent to the color-corrected SPIRE spectrum of

which the energy index was measured as  $\alpha = 1.13 \pm 0.04$ . At least in the range of  $\alpha = 0-2$ , the impact of the color correction is negligible (i.e.,  $f_{\text{col}} = 0.99-1.00$ ) for all the three SPIRE bands.

**Table 1.** SPIRE photometry of the west hot spot of Pictor A.

$\lambda$ ( $\mu\text{m}$ ) <sup>a</sup>	$F_\nu$ (mJy) <sup>b</sup>	$\Delta F_{\nu,\text{sys}}$ (mJy) <sup>c</sup>	$f_{\text{col}}$ <sup>d</sup>
250	$63.3 \pm 10.7$	3.5	1.0003
350	$70.0 \pm 9.9$	3.9	1.0004
500	$123.7 \pm 10.9$	6.8	0.9995

<sup>a</sup>The effective wavelength.

<sup>b</sup>The color-corrected flux density.

<sup>c</sup>The systematic error of the SPIRE photometry (5.5%; Bendo et al. 2013; Pearson et al. 2014).

<sup>d</sup>The adopted color-correction factor.

## 3. SPECTRAL ENERGY DISTRIBUTION

### 3.1. FIR excess

Figure 2 compiles the spectral energy distribution of the synchrotron radiation from the west hot spot of Pictor A in the radio-to-optical frequency range (Meisenheimer et al. 1997; Wilson et al. 2001; Tingay et al. 2008; Werner et al. 2012; Isobe et al. 2017). The best-fit PL model to the radio data in the 330 MHz–233 GHz range with an energy index of  $\alpha = 0.74 \pm 0.015$  (Meisenheimer et al. 1997) is shown with the hatched tie in panel (a) of Figure 2. The PL-like radio spectrum appears to be smoothly connected to the optical data points, with a cutoff at  $\nu \gtrsim 10^{14}$  Hz. However, Isobe et al. (2017) unveiled that the MIR flux measured with *WISE* and *Spitzer* (Werner et al. 2012) significantly exceeds the extrapolation of the radio spectrum especially at  $\nu \lesssim 3 \times 10^{13}$  Hz (i.e.,  $\lambda \gtrsim 10 \mu\text{m}$ ). They tried to reproduce the radio-to-optical synchrotron spectrum of the object by a double cutoff-PL model, as shown in panel (b) of Figure 2. The main cutoff-PL component (the dotted line in panel b of Figure 2) dominates the flux in the radio and optical bands, while the second cutoff-PL one (the dashed line) was introduced to reproduce the MIR excess.

Panel (a) of Figure 2 clearly displays that the FIR flux obtained with the *Herschel* SPIRE (the filled circles) is significantly higher than the PL model fitted to the radio data. This strongly indicates that the excess has a significant contribution not only in the MIR

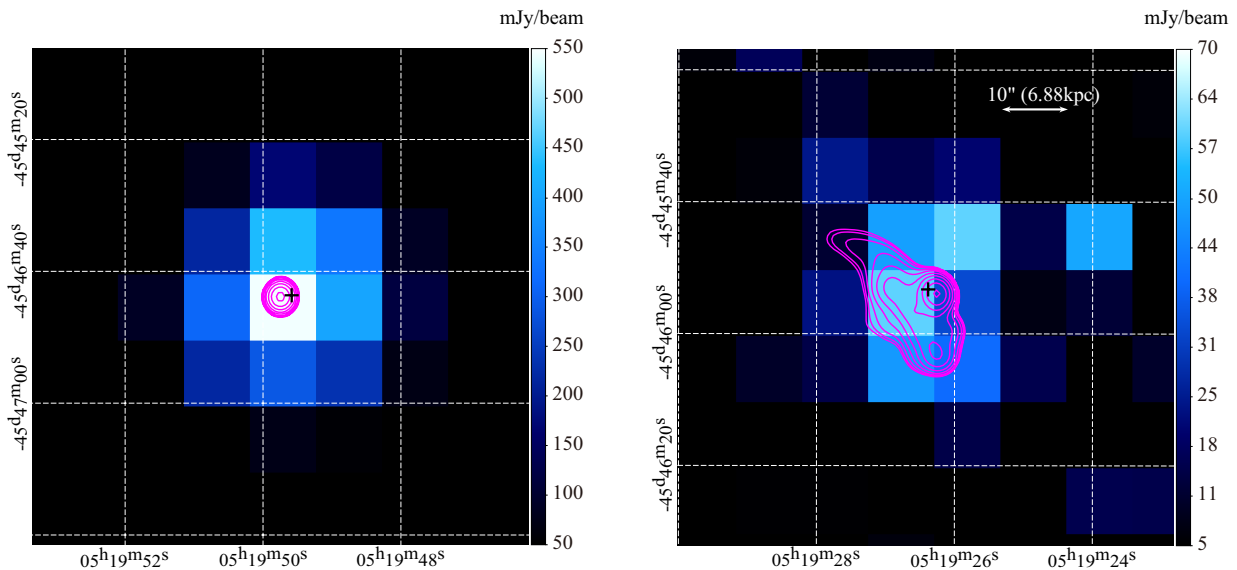


**Figure 1.** SPIRE Level-2 point-source maps at  $350 \mu\text{m}$  around the nucleus (left) and west hot spot (right) of the radio galaxy Pictor A. The color scale in the individual panels indicates the FIR intensity in the unit of  $\text{mJy beam}^{-1}$ , where the  $350 \mu\text{m}$  SPIRE beam size is  $24.2''$  in the full width at half maximum. The 4.8 GHz ATCA image is overlaid with contours. The major and minor radii of the ATCA beam are evaluated as  $1.17''$  and  $1.25''$ , respectively. The cross in the individual panels shows the  $350 \mu\text{m}$  SPIRE position of the nucleus and hot spot. The horizontal arrow in the right panel corresponds to the angular size of  $10''$  ( $6.88 \text{ kpc}$  at the source rest frame).

range but also in the FIR one. As shown in panel (b), the double cutoff-PL model by *Isobe et al. (2017)* is still inadequate to describe the FIR data. Therefore, the spectral shape of the FIR-to-MIR excess requires to be re-modeled. The FIR excess flux in the SPIRE range is summarized in Table 2. By adopting the model parameters presented in *Isobe et al. (2017)*, the excess flux density above the main component is evaluated as  $F_{\nu, \text{ex1}} = 33.4 \pm 9.9 \text{ mJy}$  at the wavelength of  $350 \mu\text{m}$ , while that above the double cutoff-PL model is estimated as  $F_{\nu, \text{ex2}} = 18.4 \pm 9.9 \text{ mJy}$ . It is impossible to ascribe the FIR excess to the systematic uncertainty in the SPIRE photometry,  $\Delta F_{\nu, \text{sys}} = 3.9 \text{ mJy}$  at  $350 \mu\text{m}$  (typically 5.5%; *Bendo et al. 2013; Pearson et al. 2014*).

**Table 2.** The FIR excess flux measured with the SPIRE.

$\lambda$ ( $\mu\text{m}$ )	250	350	500
$F_{\nu, \text{ex1}}$ (mJy) <sup>a</sup>	$35.2 \pm 10.7$	$33.4 \pm 9.9$	$75.4 \pm 10.9$
$F_{\nu, \text{ex2}}$ (mJy) <sup>b</sup>	$22.1 \pm 10.7$	$18.4 \pm 9.9$	$58.1 \pm 10.9$

<sup>a</sup>The excess flux over the main cutoff-PL component of *Isobe et al. (2017)*.

<sup>b</sup>The excess flux over the total model of *Isobe et al. (2017)*.

### 3.2. Rough evaluation on the spectrum of the excess

It is proposed by *Isobe et al. (2017)* that the excess component originates in the 10-pc scale substructures within the west hot spot resolved by the VLBA (*Tingay et al. 2008*), while the main component is attributed to the integrated emission all over the object. Based on this two-zone scenario, the spectrum of the excess is re-evaluated below.

In order to roughly grasp the spectral shape, a simple two-point spectral index between the frequencies  $\nu_1$  and  $\nu_2$ , defined as

$$\alpha_{\nu_1 - \nu_2} = -\frac{\log F_{\nu}(\nu_1) - \log F_{\nu}(\nu_2)}{\log \nu_1 - \log \nu_2}, \quad (1)$$

is generally useful. First, the two-point index between the FIR and MIR bands is evaluated. Here, the excess flux over the main component (i.e.,  $F_{\nu, \text{ex1}}$  in Table 2) is adopted. With the spectral parameters taken from *Isobe et al. (2017)*, the flux density of the excess in the *WISE* range is calculated as  $F_{\nu, \text{ex1}} = 5.79 \pm 0.76 \text{ mJy}$  at  $\nu = 1.36 \times 10^{13} \text{ Hz}$  ( $\lambda = 22 \mu\text{m}$ ). A comparison of the SPIRE and *WISE* flux yields the FIR-to-MIR two-point spectral index of the excess as  $\alpha_{\text{F-M}} \simeq 0.6\text{--}0.8$ .

Next, the low-frequency index below the SPIRE frequency range is estimated. As the radio intensity of the excess, the sum of the VLBA flux density of the substructures, calculated as  $F_{\nu} = 121.3 \pm 5.8 \text{ mJy}$  at 1.67 GHz after *Tingay et al. (2008)*, is adopted. This flux density is indicated with the filled triangle in Figure 2.

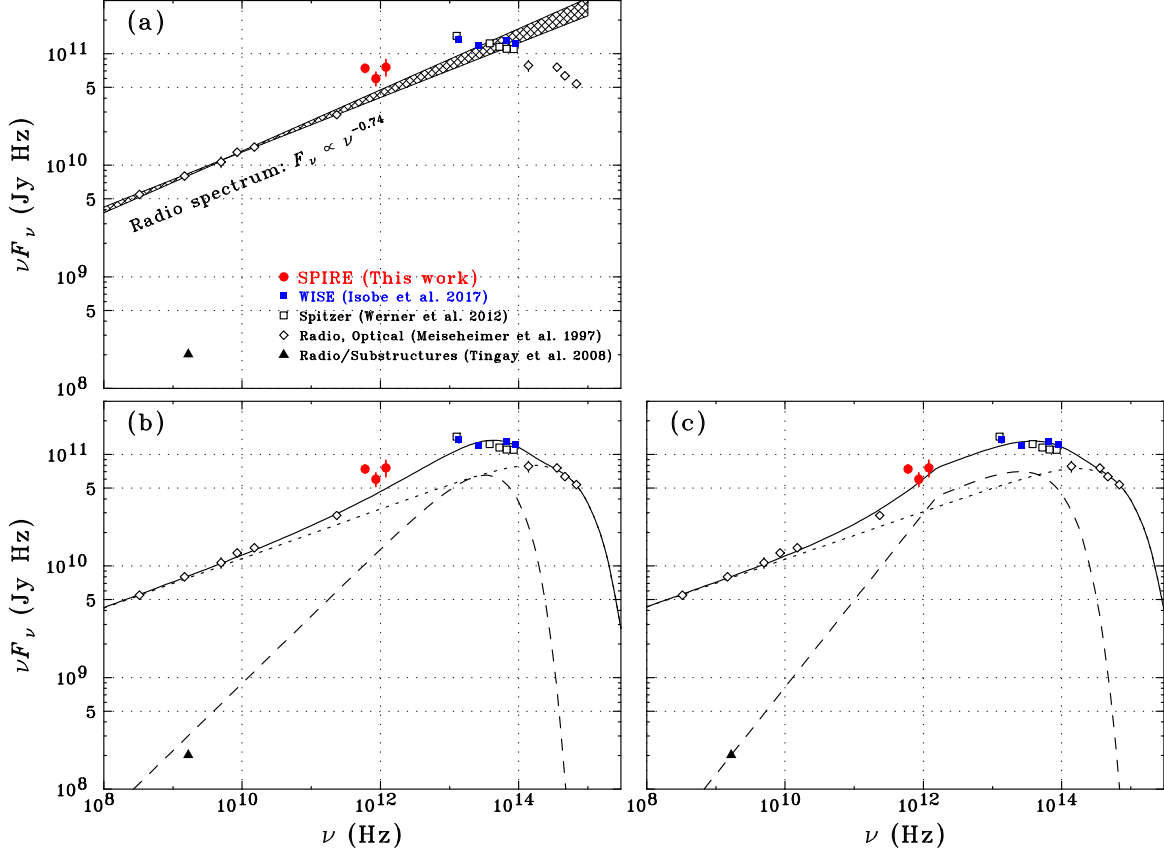


**Figure 2.** Synchrotron spectral energy distribution of the west hot spot of Pictor A in the radio-to-optical range. The filled circles indicate the FIR data taken with the *Herschel* SPIRE, while the filled and open boxes show the MIR data with *WISE* (Isobe et al. 2017) and *Spitzer* (Werner et al. 2012), respectively. The radio and optical data (Meisenheimer et al. 1997) are plotted with the open diamonds. The filled triangle indicates the 1.67 GHz VLBA flux summed over the substructures within the west hot spot (Tingay et al. 2008). In panel (a), the best-fit PL model to the radio data from 330 MHz to 233 GHz is shown with the hatched tie. The solid line in panel (b) corresponds to the double cutoff-PL model by Isobe et al. (2017), which is composed of the main (dotted line) and excess (dashed line) components. Panel (c) visualizes that the composite model (Case 2 in Table 3), where the broken-PL model is adopted for the excess with the radio flux fixed at the total flux of the substructures (i.e., 121.3 mJy, the filled triangle), successfully reproduced the radio-to-optical spectrum.

By connecting the SPIRE and VLBA data, the spectral slope between the radio and FIR bands is evaluated as  $\alpha_{R-F} \simeq 0.1-0.2$ .

A comparison of the two indices,  $\alpha_{R-F}$  and  $\alpha_{F-M}$ , strongly suggests that the excess exhibits a spectral break around the SPIRE frequency range. It is important to note that the difference between the two indices,  $\Delta\alpha = \alpha_{F-M} - \alpha_{R-F} \simeq 0.5$ , seems consistent to the radiative cooling break under the continuous energy injection (e.g., Carilli et al. 1991).

### 3.3. Spectral Modeling

Based on the argument of the two-point index, the cutoff-PL model to the excess adopted in Isobe et al. (2017) is replaced with a broken-PL model subjected to a high-frequency cutoff (hereafter, simply referred to as the broken-PL model). The cooling break condition

under the continuous injection, i.e.  $\Delta\alpha = 0.5$  at the break, is applied to the broken-PL model.

The SPIRE data, in combination with the radio, MIR and optical one, are examined by the two-component model consisting of the main cutoff-PL and excess broken-PL components. With the normalization of the excess component left free, a reasonable solution is obtained by the composite model. The resultant spectral parameters are listed in Table 3 (Case 1). All the parameters of the main component stay unchanged within errors from those in Isobe et al. (2017). The model yields the 1.67 GHz flux density and energy index below the break of the excess component as  $F_\nu = 55_{-47}^{+327}$  mJy and  $\alpha_{low} = 0.10 \pm 0.32$ , respectively. The derived flux density agrees with the sum flux density of the VLBA substructures (i.e., 121.3 mJy at 1.67 GHz). This result supports the idea that the FIR-to-MIR excess is produced in the substructures.



**Table 3.** Spectral parameters derived by the two-component model.

Component	Model	Parameter	Case 1	Case 2
Main	cutoff-PL	$F_\nu(5 \text{ GHz}) \text{ (Jy)}$ <sup>a</sup>	$2.03 \pm 0.12$	$1.98 \pm 0.09$
		$\alpha$ <sup>b</sup>	$0.78 \pm 0.02$	$0.79 \pm 0.02$
		$\nu_c \text{ (} 10^{14} \text{ Hz)}$ <sup>c</sup>	$7.1^{+3.5}_{-2.3}$	$8.0^{+3.9}_{-2.6}$
Excess	broken-PL	$F_\nu(1.67 \text{ GHz}) \text{ (mJy)}$ <sup>d</sup>	$55^{+327}_{-47}$	121.3 (fix)
		$\alpha_{\text{low}}$ <sup>e</sup>	$0.10 \pm 0.32$	$0.22 \pm 0.06$
		$\nu_b \text{ (} 10^{12} \text{ Hz)}$ <sup>f</sup>	$0.9^{+7.2}_{-0.8}$	$1.6^{+3.0}_{-1.0}$
		$\nu_c \text{ (} 10^{13} \text{ Hz)}$ <sup>c</sup>	$6.7^{+6.3}_{-3.3}$	$8.8^{+3.4}_{-2.4}$

<sup>a</sup>The 5 GHz flux density.

<sup>b</sup>The energy index of the cutoff PL model.

<sup>c</sup>The cutoff frequency.

<sup>d</sup>The 1.67 GHz flux density.

<sup>e</sup>The spectral index below the break frequency. The index above the break is assumed to be  $\alpha_{\text{high}} = \alpha_{\text{low}} + 0.5$ .

<sup>f</sup>The break frequency.

By fixing the flux density of the excess component at the total flux density of the substructures, the composite model successfully describes the spectral energy distribution of the west hot spot, as shown in panel (c) of Figure 2 where the main cutoff-PL and excess broken-PL components are drawn with the dotted and dashed lines, respectively. Table 3 tabulates the derived spectral parameters (Case 2). It is suggested that both components exhibit a comparable flux in the FIR-to-MIR frequency range (namely in  $10^{12}$ – $5 \times 10^{13}$  Hz), while the excess has only a minor contribution below the SPIRE frequency range. The break frequency of the excess is measured as  $\nu_b = 1.6^{+3.0}_{-1.0} \times 10^{12}$  Hz. The low-frequency index below this break, determined as  $\alpha_{\text{low}} = 0.22 \pm 0.06$ , becomes consistent to the two-point index,  $\alpha_{\text{R-F}} \simeq 0.1$ – $0.2$ . The cutoff frequency of the excess,  $\nu_c = 8.8^{+3.4}_{-2.4} \times 10^{13}$  Hz, is an order of magnitude lower than that of the main component,  $\nu_c = 8.0^{+3.9}_{-2.6} \times 10^{14}$  Hz. In comparison to the the cutoff-PL modeling by *Isobe et al. (2017)*, the cutoff frequency of the excess becomes slightly higher.

## 4. DISCUSSION

### 4.1. Overview of the SPIRE results

On the serendipitous maps obtained with the *Herschel* SPIRE photometer, the FIR counterpart of the west hot spot of the radio galaxy Pictor A has been discovered with a color-corrected  $350 \mu\text{m}$  flux density of  $F_\nu = 70.0 \pm 9.9$  mJy. A careful investigation of the radio-to-optical synchrotron spectral energy distribution shown in Figure 2 reveals that the MIR excess detected

with *WISE* and *Spitzer* (*Isobe et al. 2017*) significantly extends into the FIR range.

The spectral energy distribution of the object between the radio and optical bands is re-analyzed by the two-zone model, comprised of the main and excess components. Owing to the SPIRE data, it is found that the spectrum of the excess is better reproduced by the broken-PL model rather than the simple cutoff-PL one, while the spectral shape of the main component agrees with the result of *Isobe et al. (2017)* within the errors. On the condition of the radiative cooling under the continuous energy injection (i.e.,  $\Delta\alpha = 0.5$ ; *Carilli et al. 1991*), the broken-PL model becomes consistent to the scenario that the 10-pc scale substructures within the hot spot detected with the VLBA (*Tingay et al. 2008*), of which the integrated flux is 121.3 mJy, is the generator of the FIR-to-MIR excess. Based on this idea, the break frequency and low-frequency index of the excess is determined as  $\nu_b = 1.6^{+3.0}_{-1.0} \times 10^{12}$  Hz and  $\alpha_{\text{low}} = 0.22 \pm 0.06$ , respectively (Case 2). In the following, by making the most of the derived spectral parameters, the physical condition to produce the FIR-to-MIR excess is discussed.

The shortest baseline of  $l = 236$  km between Pie Town and Los Alamos adopted in the VLBA observation by *Tingay et al. (2008)* corresponds to an angular scale of  $\arctan(\lambda/l) = 0.16''$  ( $\sim 100$  pc at the redshift of Pictor A) at the wavelength of  $\lambda = 18$  cm (i.e., 1.67 GHz). As a result, this VLBA observation is likely insensitive to a spatial structure roughly larger than a few 100 pc. Thus, the 10-pc scale substructures may represent only a tip

of a larger spatial structure. For a quantitative evaluation on the interpretation that the 100-pc scale region is the source of the excess, the following constraints on the radio flux and energy index are adopted from the spectral modeling (Case 1);  $F_\nu < 382$  mJy at 1.67 GHz and  $\alpha_{\text{low}} < 0.42$ , respectively.

## 4.2. Magnetic field estimates

### 4.2.1. Minimum energy condition

The minimum-energy condition (e.g., Miley 1980) is widely adopted to quantify the magnetic field strength in synchrotron-emitting sources, especially when their inverse-Compton emission is not yet observed. The spectral properties of well-studied hot spots are reported to be successfully explained by the minimum-energy magnetic field  $B_{\text{me}}$  (e.g., Hardcastle et al. 2004; Kataoka & Stawartz 2005).

Here, the  $B_{\text{me}}$  value of the substructures are evaluated, since they are regarded as the origin of the FIR-to-MIR excess. The radio properties of the individual substructures taken from Tingay et al. (2008) are tabulated in Table 4. The VLBA image indicates that the minor axis of the substructures roughly corresponds to the direction of the jet from the Pictor A nucleus toward the west hot spot (Tingay et al. 2008). Thus, the spatial geometry of the substructures is assumed to be a simple disk, and their major and minor lengths are adopted for the diameter and thickness of the disk, respectively.

The method presented in Miley (1980) is utilized to calculate the minimum-energy magnetic field. For simplicity, a PL-like synchrotron spectrum with an index of  $\alpha_{\text{low}} = 0.22$  is adopted for all the substructures. The lower end of the synchrotron frequency is set at  $\nu_{\text{min}} = 10$  MHz by referring to Miley (1980). The hardness of the spectrum ensures that the  $B_{\text{me}}$  estimate is insensitive to  $\nu_{\text{min}}$ . The energy of the synchrotron emission is integrated up to the break frequency  $\nu_b$ . Because of the spectral break of  $\Delta\alpha = 0.5$ , the contribution of the synchrotron energy above  $\nu_b$  is regarded as negligible. The proton energy is neglected for the evaluation (i.e., the proton-to-electron energy ratio of  $k = 0$  in Miley 1980).

As shown in Table 4, the minimum-energy magnetic field is estimated as  $B_{\text{me}} = 0.25\text{--}0.43$  mG. This is found to be comparable to that of the whole west hot spot,  $B_{\text{me}} = 0.31$  mG, which is re-evaluated for  $k = 0$  from Isobe et al. (2017) by assuming a sphere geometry with a diameter of 500 pc (Wilson et al. 2001). The derived  $B_{\text{me}}$  values for the substructures and entire west hot spot are plotted against the thickness  $T$  of the region in Figure 3 (here and hereafter, the diameter is regarded as the thickness for the sphere geometry).

As briefly mentioned in §4.1, the FIR-to-MIR excess is possible to be attributed to a region larger than  $\sim 100$  pc, although such a region is potentially resolved out in the VLBA observation of Tingay et al. (2008). In order to check this interpretation, an upper limit on  $B_{\text{me}}$  is roughly estimated by utilizing those on the flux density and energy index of the excess,  $F_\nu = 382$  mJy at 1.67 GHz and  $\alpha_{\text{low}} = 0.42$  respectively. A sphere geometry is simply adopted for the evaluation. The dashed line in Figure 3 shows the  $B_{\text{me}}$  upper limit as a function of the source thickness. At  $T = 200$  pc, the constraint on the minimum-energy magnetic field is given as  $B_{\text{me}} < 0.32$  mG.

### 4.2.2. Cooling break

A more reliable estimate of the magnetic field is derived by assuming that the spectral break is caused by the radiative cooling. At the cooling break, the electron radiative cooling timescale  $t_{\text{rad}} = \frac{3m_e c}{4u_B \sigma_T \gamma}$  becomes equal to the adiabatic loss timescale  $t_{\text{ad}} = \frac{T}{v}$ , where  $\gamma$  is the Lorentz factor of synchrotron electrons,  $m_e$  is the electron rest mass,  $u_B = \frac{B^2}{8\pi}$  is the energy density of the magnetic field  $B$ ,  $\sigma_T$  is the Thomson cross section,  $T$  is the thickness of the source,  $v$  is the downstream flow velocity in the shock frame, and  $c$  is the speed of light (e.g., Inoue & Takahara 1996). Here, the effect of the inverse-Compton cooling is neglected based on the previous studies on the west hot spot of Pictor A (e.g., Tingay et al. 2008; Isobe et al. 2017, and references therein). Thus, the electron Lorentz factor at the cooling break is given as  $\gamma_b = \frac{6\pi m_e v c}{\sigma_T B^2 T}$ .

The cooling break was related to the cutoff frequency of the cutoff-PL model to the excess in Isobe et al. (2017). However, the SPIRE data reveals that the broken-PL model, satisfying the cooling break condition under the continuous energy injection ( $\Delta\alpha = 0.5$ ), is more appropriate to reproduce the excess. Therefore, the break frequency of the broken-PL model is actually regarded as the cooling break of the excess (i.e.,  $\nu_b \propto \gamma_b^2$ ). In this case, the break frequency is converted into the magnetic field as follows;

$$B^3 \simeq \frac{27\pi e m_e v^2 c}{\sigma_T^2} T^{-2} \nu_b^{-1}, \quad (2)$$

where  $e$  denotes the elementary charge. Instead, the cutoff frequency  $\nu_c$  is thought to reflect the maximum Lorentz factor of the accelerated electrons.

The area enclosed by the thin solid lines on Figure 3 displays the acceptable range of the magnetic field strength, which is estimated from the break frequency of the excess,  $\nu_b = 1.6_{-1.0}^{+3.0} \times 10^{12}$  Hz, as a function of the region size  $T$ . The flow velocity of  $v = 0.3c$  is

**Table 4.** Estimates of the minimum-energy magnetic field.

Component	$F_\nu(1.67 \text{ GHz})$ (mJy) <sup>a</sup>	Diameter (pc) <sup>a</sup>	Thickness (pc) <sup>a</sup>	$B_{\text{me}}$ (mG)
Substructure A <sup>b</sup>	$28.3 \pm 2.8$	170	42	0.31
Substructure B <sup>b</sup>	$25.9 \pm 2.6$	87	46	0.43
Substructure C <sup>b</sup>	$24.9 \pm 2.5$	127	43	0.35
Substructure D <sup>b</sup>	$6.0 \pm 0.6$	138	28	0.25
Substructure E <sup>b</sup>	$36.2 \pm 3.6$	122	58	0.36
West hot spot <sup>c</sup>	—	—	—	0.31

<sup>a</sup>Taken from [Tingay et al. \(2008\)](#).

<sup>b</sup>A disk geometry is adopted.

<sup>c</sup>A sphere geometry with a diameter of 500 pc ([Wilson et al. 2001](#)) is adopted.

employed for evaluation, as a representative value of jet-terminal shocks in radio galaxies (e.g., [Kino & Takahara 2004](#)). When the FIR-to-MIR excess is interpreted by the substructures with a thickness of  $T = 28\text{--}58$  pc, its magnetic field is limited as  $B \simeq 1\text{--}4$  mG, as shown with the hatched quadrangle on Figure 3. If the emission region of the excess is larger than these substructures, a weaker magnetic field is required (e.g.,  $B = 0.5\text{--}1$  mG at  $T = 200$  pc)

With the refined spectral investigation enabled by the SPIRE data, the magnetic field strength higher than the minimum-energy value of the substructures, originally suggested by [Isobe et al. \(2017\)](#), is reconfirmed as  $B \simeq (3\text{--}10)B_{\text{me}}$ . Even if the excess is assumed to come from the larger region with  $T > 100$  pc, a comparison of the thin solid and dashed lines on Figure 3 indicates that the magnetic field is stronger than  $B_{\text{me}}$  at least by a factor of  $\sim 1.5$ . Since the minimum-energy condition is nearly equivalent to the energy equipartition between synchrotron-emitting electrons and magnetic field, the magnetic energy density of the excess is expected to be higher than the non-thermal electron one roughly by a factor of  $(B/B_{\text{me}})^4 = 3^4\text{--}10^4$  (or at least  $\sim (1.5)^4$ ).

#### 4.2.3. Possible interpretation

Because it is difficult to ascribe such a high magnetic dominance to a simple plasma compression at the shock alone, some other physical processes, which selectively enhance the magnetic field, are required. Theoretical studies indicate that the magnetic field in the downstream region of the shock is locally amplified by turbulence induced by plasma instabilities and/or inhomogeneities. In the case of non-relativistic strong shocks, a magnetic-field amplification by more than two orders of magnitude is widely predicted by analytical calculations (e.g., [Fraschetti 2013](#)) and magnetohydrodynamic

(MHD) simulations (e.g., [Inoue et al 2009](#); [Sano et al. 2012](#); [Ji et al. 2016](#)). A similar level of magnetic-field boost is reported even in MHD simulations for relativistic shocks (e.g., [Inoue et al 2011](#)). This mechanism is invoked to explain the magnetic field inferred for X-ray shells/rims ( $\sim 100 \mu\text{G}$ , [Vink & Laming 2004](#); [Bamba et al. 2003](#)) and X-ray hot spots ( $\sim 1$  mG, [Uchiyama et al. 2007](#)) found in supernovae remnants, since these magnetic fields are significantly stronger than the interstellar field (a few  $\mu\text{G}$ ). Therefore, it is natural to infer that regions with an amplified magnetic field residing in the post-shock medium inside the west hot spot are observed as the substructures from which the FIR-to-MIR synchrotron excess is radiated.

### 4.3. Electron acceleration process

#### 4.3.1. Doubt as to the standard shock scenario

It is widely believed that the particles are efficiently accelerated by the jet-terminal shock via the first-order Fermi process in the hot spots of radio galaxies ([Begelman et al. 1984](#)). It is theoretically shown that this acceleration process produces a non-thermal electron population with a PL-shaped energy distribution function described as  $N(\gamma) \propto \gamma^{-p}$  (e.g., [Drury 1983](#)), in the  $\gamma$  range where the radiative cooling is insignificant. In the non-relativistic case, the spectrum of the accelerated electrons becomes hardest at the strong shock limit with the index of  $p = 2$ , which corresponds to the synchrotron index of  $\alpha = 0.5$  (i.e.,  $p = 2\alpha + 1$ ). For relativistic strong shocks, the electron spectrum is suggested to be slightly softer as  $p = 2.2\text{--}2.4$  (e.g., [Kirk et al. 2000](#); [Achterberg et al. 2001](#); [Spitkovsky 2008](#)). Therefore, the standard strong-shock picture is unable to create the flat electron spectrum with  $p = 1.44 \pm 0.12$ , required for the 10-pc substructure to reproduce the FIR-to-MIR excess with  $\alpha_{\text{low}} = 0.22 \pm 0.06$ . Even if the 100-pc scale



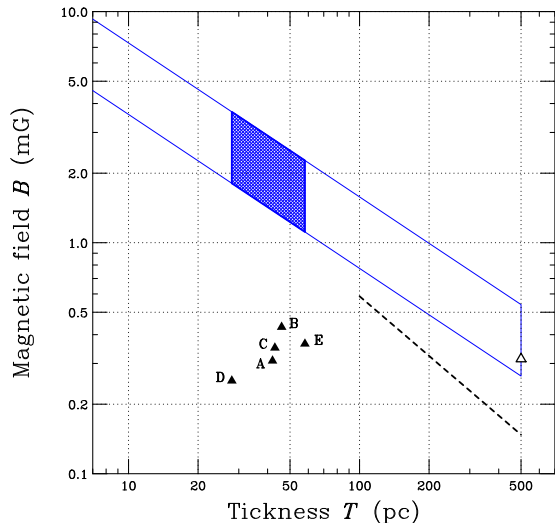


**Figure 3.** Constraints on the magnetic field  $B$  of the FIR-to-MIR excess observed from the west hot spot, as a function of the thickness (or the sphere diameter)  $T$  of the emission region. The filled and open triangles indicate the minimum-energy magnetic field,  $B_{\text{me}}$ , of the substructures (denoted as A, B, C, D and E) and entire west hot spot, respectively. The dashed line shows the  $B_{\text{me}}$  upper limit for the large source with  $T > 100$  pc, estimated from the constraints on the flux density of the excess ( $F_\nu < 382$  mJy at 1.67 GHz) and on the energy index ( $\alpha_{\text{low}} < 0.42$ ). The magnetic field of the excess, estimated by inputting the measured break frequency of  $\nu_b = 1.6^{+3.0}_{-1.0} \times 10^{12}$  Hz into Equation (2), is shown with the thin solid line. For the estimation, a representative downstream flow velocity of  $v = 0.3c$  (Kino & Takahara 2004) is adopted. The upper bound on  $T$  corresponds to the diameter of the west hot spot (500 pc; Wilson et al. 2001). When the excess is assumed to originate in the VLBA substructures with a thickness of  $T = 28\text{--}58$  pc (Tingay et al. 2008), the magnetic field required by the excess is restricted to be within the hatched area.

source is considered, the spectrum ( $\alpha_{\text{low}} < 0.42$  and hence  $p < 1.84$ ) is still harder than the prediction by the strong shock. In the following, two alternatives are discussed as a viable mechanism to make a hard spectrum with  $p < 2$  and hence  $\alpha < 0.5$ ; *stochastic acceleration via magnetic turbulence* and *acceleration by magnetic reconnection*.

#### 4.3.2. Stochastic acceleration

Within magnetized plasma flows, particles are expected to be powered by magnetic turbulence (e.g., Schlickeiser 1984; Howes 2010). The particle acceleration through the magnetic turbulence, usually called as the stochastic acceleration, is phenomenologically equivalent to the second-order Fermi acceleration. This mechanism was applied to gamma-ray bursts (e.g., Asano & Terasawa 2009, 2015) of which the spectrum is conventionally approximated by the so-called Band

function (Band et al. 1993), and to gamma-ray blazars (e.g., Asano & Hayashida 2018), especially those with an exceptionally hard spectrum (Asano et al. 2014). The stochastic acceleration seems compatible to the magnetic amplification presented in §4.2.3. It is suggested that the synchrotron electrons in the X-ray hot spots of the supernovae remnants, where the magnetic field is possibly strengthened by turbulence, are energized by the in-situ stochastic acceleration (Inoue et al. 2009).

By referring to the simple review by Asano et al. (2014), the stochastic acceleration is applied to the FIR-to-MIR excess from the west hot spot of Pictor A. The electron spectrum obtained by the stochastic acceleration is controlled by the turbulence spectrum. In the standard manner, the spectrum of the turbulent magnetic field is written as  $\delta B^2 \propto k^{-q}$ , where  $k$  is the wave number of the turbulence. In the steady state, the spectrum of the accelerated electrons converges on the PL form as  $N(\gamma) \propto \gamma^{-(q-1)}$  (i.e.,  $p = q - 1$ ), if the effect of electron escape from the acceleration region is neglected. The Kolmogorov turbulence (Kolmogorov 1941), which is often observed in natural phenomena, is represented by  $q = 5/3$ . In this case, a "rising" synchrotron spectrum with  $\alpha = -1/6$  ( $p = 2/3$ ) is anticipated, although such a very hard spectrum is rarely observed from synchrotron objects. The value of  $q > 2$  is thought to be unphysical, since the acceleration time scale ( $\propto \gamma^{-(q-2)}$ ) becomes shorter for higher energy particles. Therefore, the softest spectrum is obtained in the hard-sphere condition with  $q = 2$ , corresponding to  $p = 1$  and  $\alpha = 0$ , where the acceleration time scale is independent of the electron energy. It is reported that the hard-sphere-like turbulence is achieved in the presence of energy transfer from small to large scales (inverse transfer, Brandenburg et al. 2015).

The synchrotron and corresponding electron spectra of the FIR-to-MIR excess,  $\alpha_{\text{low}} = 0.22$  and  $p = 1.44$ , respectively (or  $\alpha_{\text{low}} < 0.42$  and  $p < 1.84$  in the case of the 100-pc scale source) are still slightly softer than the prediction for the hard-sphere condition ( $\alpha = 0$  and  $p = 1$ ). In other words, the index of the turbulence required for the excess,  $q = 2.44$  (or  $q < 2.84$ ), appears to be within the unphysical range. In order for the stochastic acceleration to be acceptable, some other processes are necessary to steepen the electron spectrum.

The above argument neglects, for simplicity, the effect of the electron escape from the acceleration region. It is confirmed in numerical studies (e.g., Becker et al. 2006) that the spectrum becomes softened by taking the electron escape into account, since the escape time scale is shorter for higher energy particles. Thus, the stochastic

acceleration accompanied by the particle escape is proposed as one of the plausible mechanisms for the FIR-to-MIR excess.

### 4.3.3. Magnetic reconnection

Another important process, which invokes energy dissipation from the magnetized plasma flow into high-energy particles, is provided by magnetic reconnection (e.g., Rowan et al. 2017). The plasma heating and particle acceleration caused by the magnetic reconnection is actually observed in solar flares (e.g., Tsuneta et al. 1992). There are numbers of application of the magnetic reconnection to high energy phenomena in various kinds of astrophysical objects, including pulsar wind nebulae (e.g., Lyubarsky & Kirk 2001), jets from active galactic nuclei (e.g., Romanova & Lovelace 1992), and gamma-ray bursts (e.g., Zhang & Yan 2011).

In order to characterize the magnetized flow, the magnetization parameter is widely utilized. In theoretical studies of electron-positron pair plasma (e.g., Guo et al. 2014, 2015; Sironi & Spitkovsky 2014; Werner et al. 2016), the magnetization parameter is defined as  $\sigma = B^2/(4\pi n_e m_e c^2)$  where  $n_e$  is the number density of electrons and positrons. This parameter quantifies the relative dominance of the magnetic energy density to the electron rest-mass one in the flow. The electron acceleration by the magnetic reconnection is predicted to effectively work for the highly magnetized condition of  $\sigma \gg 1$ . The strong magnetic field of  $B/B_{\text{me}} \simeq (3\text{--}10)$  estimated for the substructure from the excess (or  $\gtrsim 1.5$  for the 100-pc scale emission region) is reminiscent of the high magnetization.

One of the remarkable properties of the reconnection acceleration is that the process is able to easily construct a hard PL spectrum with an electron index of  $p < 2$ . It is widely predicted by particle-in-cell simulations (e.g., Guo et al. 2014, 2015; Sironi & Spitkovsky 2014; Werner et al. 2016) that the hardness of the electron spectrum is clearly dependent on the magnetization; the higher  $\sigma$  value tends to give the flatter spectral index. Based on these simulations, the spectral index of the FIR-to-MIR excess ( $p = 1.44$  and  $\alpha_{\text{low}} = 0.22$ ) appears to be achieved in the magnetization of  $\sigma = 10\text{--}50$ . Even though the soft end of the derived index ( $p < 1.84$  and  $\alpha_{\text{low}} < 0.42$ ) is adopted, the magnetization parameter of at least  $\sigma > 5$  is necessary.

A difficulty of the reconnection interpretation is found in the highest electron Lorentz factor. The numerical studies indicate that the magnetic reconnection with  $\sigma = 10\text{--}50$  is possible to accelerate the electrons up to the maximum Lorentz factor of  $\gamma_{\text{max}} \simeq 100$  (Werner et al. 2016) or at most  $\lesssim$

3000 (Sironi & Spitkovsky 2014). These values are highly surpassed by the Lorentz factor corresponding to the cutoff frequency of the excess,  $\gamma_c = 1.9 \times 10^5 (B/2 \text{ mG})^{-0.5} (\nu_c/8.8 \times 10^{13} \text{ Hz})^{0.5}$ . The overall synchrotron spectrum of the excess is unattributable to the simple magnetic reconnection alone. This problem may get severer, if the origin of the excess is the 100-pc scale substructures, since the lower  $\gamma_{\text{max}}$  value is anticipated for the weaker magnetization.

An interesting idea to overcome this problem is presented in Werner et al. (2016). In the standard theoretical/numerical studies, the reconnection is assumed to be induced by cold injection flows. If the reconnection is caused by "hot" injection flows with an average electron Lorentz factor of  $\bar{\gamma}$ , the maximum Lorentz factor is expected to be boosted by a factor of  $\bar{\gamma}$  (i.e.,  $\gamma_{\text{max,hot}} = \bar{\gamma}\gamma_{\text{max}}$ ). In order to interpret the excess by the reconnection, the average Lorentz factor of the hot injection flow is requested to be in the range of  $\bar{\gamma} = 100\text{--}1000$  ( $\sim \gamma_c/\gamma_{\text{max}}$ ). Therefore, the reconnection accompanied by some pre-heating/acceleration mechanisms is possible to give a solution to the spectrum of the excess.

The origin of the excess, regardless of its spatial scale, basically resides in the west hot spot. Thus, the strong shock, which is a source of the main synchrotron component of the west hot spot, is possible to supply the hot injection flow. Another source of the pre-acceleration is potentially provided by the substructures themselves. It is generally considered in theoretical studies (e.g., Quataert & Gruzinov 1999; Lazarian & Vishniac 1999; Lazarian et al. 2004; Zhang & Yan 2011; Chael et al. 2018, 2019) that the magnetic turbulence is mediated by the reconnection. Therefore, it is inferred that the reconnection and stochastic accelerations are concurrent in the magnetized plasma. If this is the case, the stochastic acceleration in the substructures acts as the pre-accelerator.

In summary, the very hard spectrum of the FIR-to-MIR excess observed from the west hot spot of Pictor A is ascribed to the stochastic acceleration and/or magnetic reconnection. Both processes are thought to have a compatibility to the magnetic amplification by the turbulence, which is proposed to explain the strong magnetic field of the excess. A further support for this idea will be given by numerical/analytical evaluation of the acceleration-related parameters, although it is out of scope of the present study.

### 4.4. Implications for the origin of the X-ray emission

Finally, the possible mechanism for the X-ray emission and its relation to the FIR-to-MIR excess are briefly discussed. In spite of the extensive multi-frequency studies

of the west hot spot of Pictor A, no unified picture has been yet constructed for the origin of its X-ray photons. Because of the X-ray slope ( $\alpha_X = 1.07 \pm 0.11$ , Wilson et al. 2001) significantly steeper than the synchrotron radio one and of the unusually high X-ray-to-radio flux ratio, it is difficult to reproduce simultaneously the X-ray and radio-to-optical spectra by the standard one-zone SSC model, even if the FIR-to-MIR excess is neglected. In order to overcome this problem, a number of multi-component interpretations were attempted (e.g., Wilson et al. 2001; Tingay et al. 2008).

The new population of non-thermal electrons possibly localized in the substructures within the hot spot is identified in the present study through the discovery of the FIR-to-MIR synchrotron excess. However, considering the hardness of the excess ( $\alpha_{\text{low}} = 0.22 \pm 0.06$  or conservatively  $\alpha_{\text{low}} < 0.42$ ), the inverse-Compton emission by this additional electron component is unable to give a meaningful solution to the X-ray spectrum, regardless of its seed photon source.

It is proposed in Tingay et al. (2008) that the X-ray spectrum of the west hot spot of Pictor A is created by the substructures via the synchrotron radiation. They overcame the problem of the X-ray softness by assuming that the synchrotron break/cutoff is located around the X-ray band. In order to make the idea of Tingay et al. (2008) compatible to the result of the present study, the substructures are requested to produce two independent synchrotron electron populations; one for the FIR-to-MIR excess and the other for the X-ray photons. Because these two components exhibit a very different spectral shape from each other, the acceleration conditions in the individual substructures are possible to be heterogeneous.

When the mG-level magnetic field in the substructures required to explain the FIR-to-MIR excess is applicable to the X-ray emitting region, the synchrotron cooling time scale of the X-ray electrons is evaluated as  $t_{\text{sync}} \sim 1 \text{ yr } (B/2 \text{ mG})^{-1.5} (E_X/1 \text{ keV})^{-0.5}$  where  $E_X$  is the X-ray synchrotron photon energy. This time scale is consistent to the observational fact that the hot spot showed an X-ray flux decrease by 10% in 3 months (Hardcastle et al. 2016). In contrast, the electron cooling time scale at the break of the excess is significantly longer as  $t_{\text{sync}} \sim 450 \text{ yr } (B/2 \text{ mG})^{-1.5} (\nu_b/1.6 \times 10^{12} \text{ Hz})^{-0.5}$ . The longer timescale is consistent to the MIR result that no significant flux variation is detected between the *Spitzer* and *WISE* observations with an interval of  $\sim 5$  years (Werner et al. 2012; Isobe et al. 2017). Thus, the substructure interpretation with a magnetic field of a few mG becomes consistent to the observed timescale of the X-ray and MIR variations. As is implied in Isobe et al.

(2017), the relatively young and elderly substructures are thought to account for the X-ray spectrum and FIR-to-MIR excess, respectively.

Another exotic multi-component idea is presented by Aharonian (2002); i.e., proton synchrotron radiation. They tried to model the X-ray spectrum of extended jet features in several radio galaxies by the proton synchrotron radiation. In their model, the soft X-ray spectrum of the west hot spot of Pictor A is interpreted by the effect of the synchrotron cooling or the proton escape. In either cases, the proton synchrotron process, when applied to the west hot spot of Pictor A, requires a magnetic field of a few mG with a source size of  $\sim \text{kpc}$ , which is comparable to the overall size of the hot spot (a diameter of 500 pc is commonly adopted in Wilson et al. 2001; Tingay et al. 2008; Isobe et al. 2017). Interestingly, this field strength is comparable to that of the substructures evaluated by the FIR-to-MIR excess. Considering the minimum-energy magnetic field of the entire west hot,  $B_{\text{me}} = 310 \mu\text{G}$  (the open triangle on Figure 3), the proton-synchrotron scenario inevitably requests the magnetic field amplification to take place all over the object.

#### 4.5. Future perspective

The present result clearly demonstrates the great potential of the FIR data for investigating the particle acceleration phenomena in the hot spots, and presumably in other jet-related features. It is interesting to mine the *Herschel* data archive for other FIR hot spots. In addition, the next generation space observatory Space Infrared Telescope for Cosmology and Astrophysics (*SPICA*; Roelfsema et al. 2018) is expected to make a great progress in this research field. These FIR data will give an answer to whether the FIR-to-MIR excess and associated physical processes are a common feature among the hot spots.

In order to make a definite conclusion to the two-zone scenario for the radio-to-optical synchrotron spectrum of the west hot spot in Pictor A, it is of crucial importance to obtain high-resolution images with a sub-arcsec resolution between the mm and FIR ranges. Such images will be utilized to specify which substructures dominate the excess. For this purpose, the Atacama Large Millimeter/submillimeter Array (ALMA) is regarded as the ideal instrument. In addition, a denser short-baseline coverage enabled by ALMA is useful to search for 100-pc scale substructures which were possibly missed in the VLBA observation by Tingay et al. (2008). Finally, polarimetric information obtained with ALMA is expected to be very useful to constrain the magnetic field configu-

ration and to infer the particle acceleration process (e.g., [Orienti et al. 2017](#)).

## ACKNOWLEDGMENTS

The authors deeply appreciate the productive comments from the anonymous referee to improve the arguments in the present paper. The authors are grateful to Dr. K. Asano for his suitable advice on the stochastic acceleration. The ATCA data of Pictor A were originally provided by Dr. E. Lenc. This research made use of the data obtained with *Herschel*, an ESA space observatory with science instruments provided by European-led Principal Investigator consortia and with important participation from NASA. The present research is supported by JSPS KAKENHI Grant Numbers JP18K03656 and JP18H03721.

## REFERENCES

- Achterberg, A., et al., 2001, *MNRAS*, 328, 393
- Aharonian, F. A., 2002, *MNRAS*, 332, 215
- Asano, K., & Terasawa, T., 2009, *ApJ*, 705, 1714
- Asano, K., & Terasawa T., 2015, *MNRAS*, 454, 2248
- Asano, K., Takahara, F., Kusunose, M., et al., 2014, *ApJ*, 780, 64
- Asano, K., & Hayashida, M., 2018, *ApJ*, 861, 31
- Bamba, A., et al., 2003, *ApJ*, 589, 827
- Band, D., Matteson, J., Ford, L. et al., 1993, *ApJ*, 413, 281
- Becker, P. A., Le, T., & Dermer, C. D., 2006, *ApJ*, 647, 539
- Begelman, M. C., Blandford, R. D., & Rees, M. J., 1984, *RvMP*, 56, 255
- Bendo, G. J., Griffin, M. J., Bock, J. J., et al., 2013, *MNRAS*, 433, 3062
- Brandenburg, A., Kahniashvili, T., & Tevzadze, A. G., 2015, *PhRvL*, 114, 5001
- Carilli, C. L., Perley, R. A. Dreher, J. W. et al., 1991, *ApJ*, 383, 554
- Chael, A., Narayan, R. J., & Michael D., 2019, *MNRAS*, 486, 2873
- Chael, A., Rowan, M., Narayan, R., et al., 2018, *MNRAS*, 478, 5209
- Drury, L. Oc., 1983, *Reports on Progress in Physics*, 46, 973-1027
- Eracleous, M., & Halpern, J. P., 2004, *ApJS*, 150, 181
- Fanaroff, B. L., & Riley, J. M., 1974, *MNRAS*, 167, 31
- Fraschetti, F., 2013, *ApJ*, 770, 84
- Griffin, M. J., Abergel, A., Abreu, A., et al., 2010, *A&A*, 518, 3
- Guo, F., Li, H., Daughton, W., et al., 2014, *PhRvL*, 113, 5005
- Guo, F., Liu, Y.-H., Daughton, W., et a;., 2015, *ApJ*, 806, 167
- Hardcastle, M. J., Harris, D. E., Worrall, D. M., et al., 2004, *ApJ*, 612, 729
- Hardcastle, M. J., Lenc, E., Birkinshaw, M., et al., 2016, *MNRAS*, 455, 3526
- Howes, G. G., 2010, *MNRAS*, 409, L104
- Inoue, S., & Takahara, F., 1996, *ApJ*, 463, 555
- Inoue, T., Yamazaki, R., & Inutsuka, S., 2009, *ApJ*, 695, 825
- Inoue, T., Asano, K., Ioka, K., 2011, *ApJ*, 734, 77
- Isobe, N., Koyama, S, Kino, M., et al., 2017, *ApJ*, 850, 193
- Ji, S., Oh, S. P., Ruszkowski, M. et al., 2016, *MNRAS*, 463, 3989
- Kataoka, J. & Stawarz, L., 2005, *ApJ*, 622, 797
- Kino, M., & Takahara, F., 2004, *MNRAS*, 349, 336
- Kraft, R. P., Birkinshaw, M., Hardcastle, M. J., et al., 2007, *ApJ*, 659, 1008
- Kirk, J. G., et al., 2000, *ApJ*, 542, 235
- Kolmogorov, A., 1941, *Akademiia Nauk SSSR Doklady*, 30, 301
- Lazarian, A., & Vishniac, E. T., 1999, *ApJ*, 517, 700
- Lazarian, A.; Vishniac, E. T., & Cho, J., 2004, *ApJ*, 603, 180
- Lyubarsky, Y., & Kirk, J. G., 2001, *ApJ*, 547, 437
- Meisenheimer, K., Roser, H.-J., Hiltner, P. R., et al., 1989, *A&A*, 219, 63
- Meisenheimer, K., Yates, M. G., & Roeser, H.-J., et al., 1997, *A&A*, 325, 57
- Miley, G., 1980, *ARA&A*, 18, 165
- Orienti, M., Brunetti, G., Nagai, H., et al. 2017, *MNRAS*, 469, L123
- Pearson, C., Lim, T., North, C., et al., 2014, *ExA*, 37, 175
- Perley, R.A., Roser, H-J. & Meisenheimer, K., 1997, *A&A*, 328, 12

- Pilbratt, G. L., Riedinger, J. R., Passvogel, T., et al., 2010, *A&A*, 518, 1
- Poglitsch, A., Waelkens, C., Geis, N., et al., 2010, *A&A*, 518, 2
- Quataert, E. & Gruzinov, A., 1999, *ApJ*, 520, 248
- Roelfsema, P. R., Shibai, H., Armus, L., et al., 2018, *PASA*, accepted (arXiv:1803.10438)
- Romanova, M. M., & Lovelace, R. V. E., 1992, *A&A*, 262, 26
- Rowan, M. E.; Sironi, L. & Narayan, R., 2017, *ApJ*, 850, 29
- Sano, T., Nishihara, ., Matsuoka, C., et al. 2012, *ApJ*, 758, 126
- Schlickeiser, R., 1984, *A&A*, 136, 227
- Sironi, L. & Spitkovsky, A., 2014, *ApJ*, 783, L21
- Spergel, D. N., Verde, L., Peiris, H. V., et al., 2003, *ApJS*, 148, 175
- Spitkovsky, A., 2008, *ApJ*, 682, L5
- Swinyard, B. M., Ade, P., Baluteau, J.-P., et al. 2010, *A&A*, 518, 4
- Thomson, R. C., Crane, P., Mackay, C. D., et al., 1995, *ApJ*, 446, 93
- Tingay, S. J., Lenc, E., Brunetti, G., et al., 2008, *AJ*, 136, 2473
- Tsuneta, S., Hara, H., Shimizu, T., et al., 1992, *PASJ*, 44, L63
- Uchiyama, Y., Urry, C. M., Cheung, C. C., et al., 2006, *ApJ*, 648, 910
- Uchiyama, Y., Aharonian, F. A., Tanaka, T., et al., 2007, *Nature*, 449, 576
- Vink, J., & Laming, J. M., 2003, *ApJ*, 584, 758
- Werner, M. W., Murphy, D. W., Livingston, J. H., et al., 2012, *ApJ*, 759, 86
- Werner, G. R., Uzdensky, D. A., Cerutti, B., et al., 2016, *ApJ*, 816, L8
- Wilson, A. S., Young, A. J., Shopbell, P. L., et al. 2001, *ApJ*, 547, 740
- Zhang, B., & Yan, H., 2011, *ApJ*, 726, 90